metals

MDPI

Article

# Microstructures and Mechanical Properties of Dissimilar Al/Steel Butt Joints Produced by Autogenous Laser Keyhole Welding

**Li Cui [1,*], Boxu Chen [1], Wei Qian [1], Dingyong He [1] and Li Chen [2]**

[1] College of Materials Science and Engineering, Beijing University of Technology, Beijing 100124, China; thecbx92@emails.bjut.edu.cn (B.C.); qwn@emails.bjut.edu.cn (W.Q.); dyhe@bjut.edu.cn (D.H.)

[2] High Energy Density Beam Processing Technology Department, Aeronautical Manufacturing Technology Research Institute, Beijing 100024, China; ouchenxi@163.com

* Correspondence: cuili@bjut.edu.cn; Tel.: +86-10-6739-2523

Received: 30 September 2017; Accepted: 8 November 2017; Published: 10 November 2017

**Abstract:** Dissimilar Al/steel butt joints of 6.0 mm thick plates have been achieved using fiber laser keyhole welding autogenously. The cross sections, interface microstructures, hardness and tensile properties of Al/steel butt joints obtained under different travel speeds and laser beam offsets were investigated. The phase morphology and thickness of the intermetallic compound (IMC) layers at the interface were analyzed by scanning electronic microscopes (SEM) using the energy-dispersive spectrometry (EDS) and electron back-scattered diffraction (EBSD) techniques. The results show that travel speeds and laser beam offsets are of considerable importance for the weld shape, morphology and thickness of IMC layers, and ultimate tensile strength (UTS) of Al/steel butt joints. This proves that the IMC layers consist of $Fe_2Al_5$ phases and $Fe_4Al_{13}$ phases by EBSD phase mapping. Increasing laser beam offsets from 0.3 mm to 0.7 mm significantly decreases the quantity of $Fe_4Al_{13}$ phases and the thickness of $Fe_2Al_5$ layers at the interface. During tensile processing, the $Fe_2Al_5$ layer with the weakest bonding strength is the most brittle region at the interface. However, an intergranular fracture that occurred at $Fe_2Al_5$ layers leads to a relatively high UTS of Al/steel butt joints.

**Keywords:** Al/steel joints; laser keyhole welding; IMC layers; tensile properties; EBSD phase mapping

## 1. Introduction

Dissimilar joining of Al/steel joints has become increasingly significant in industrial applications with a particular weight-saving interest [1,2]. Although research on joining dissimilar steel/Al alloy joints with fusion-based welding processes is extensive, most previous studies have been focused on lapped joints or overlap joints of less than 2 mm thick sheets for automotive applications [2,3]. In recent years, the development of fast-speed vessels requires improved solutions to the dissimilar joining of Al alloy superstructures to the steel hull for achieving weight reduction in the shipbuilding industry [4,5]. Thus, the dissimilar joining of thick Al/steel joints has received considerable attention in shipbuilding applications [6]. In general, an explosive Al/steel transition joint is used in the shipyard for the dissimilar joining of Al/steel joints. However, the cost of the transition joints bonded by explosive welding is high due to the complex manufacturing process [4,5,7]. Therefore, it is highly important to develop new welding process for dissimilar joining Al/steel joints directly.

It is well known that dissimilar joining Al/steel joints is extremely challenging due to the huge disparity in thermal–physical properties between steels and Al alloys [4,8,9]. One of the main issues associated with welding Al/steel joints is the formation of thick intermetallic compound (IMC) layers at the interface [10,11]. While the IMC layer is necessary for achieving a reliable Al/steel joint,

the brittleness of Al/steel joints is increased and the mechanical property is reduced if the IMC layer thickness is beyond a certain range [12,13]. The key to improving the mechanical properties of the joints is to control the formation of IMCs and limit IMCs thickness within 10 μm [14]. Therefore, considerable effort has been put into inhibiting the growth of IMC layers at the interface of Al/steel joints. The results show that welding processes allowing precise control to potentially minimize heat input (by an optimization of process parameters) are required to obtain thin IMC layers [15,16]. In view of this, a laser is regarded as a desirable heating source for joining dissimilar steel to Al alloys because of its characteristics of high power density, low welding heat input, and precise control of the location of laser focus, etc., which allow better control of the IMC layer thickness at the interface [7,17,18].

Some work has been reported on the laser welding-brazing process for dissimilar steel/Al alloy joining. During the welding, metals with a low melting point (e.g., Al alloy) and the filler wire are melted by laser or a laser-arc hybrid heating source, while metals with a high melting point (e.g., steel) is brazed by the molten metal in the solid state [1,16,17]. Thus, the resulted joint has dual characteristics: it is a welded joint on the low melting point metal side and a brazed joint on the high melting point metal side [19]. Compared to the fusion-welding processes, this process is effective for limiting the mixture of the dissimilar molten metal and inhibiting the formation of brittle IMCs at the interface. However, it is inefficient when the laser is irradiated at the low melting point Al alloy side, because Al has a high reflectivity for lasers. In addition, using laser welding–brazing can achieve an acceptable steel/Al alloy joint, but the wettability is not good when liquid Al alloy meets the solid steel. So the addition of flux, coating or other methods is usually applied to improve wettability [14,18,20,21].

Laser keyhole welding is one of the most widely used of the various laser-welding processes in dissimilar joints. With the laser keyhole-welding technique, rather good mechanical properties were obtained by irradiating steels placed on Al sheets, and limiting Al to steels mixed with a reduced steel penetration in Al alloys [8]. This indicates that the laser keyhole welding process was mainly used to lapped or overlapped joints [12,13,15,22–24]. It can be, but rarely is, used for welding Al/steel butt joints requiring accurate groove preparations, flux and filler wires [24–27]. Although the use of filler wires or flux leads to some improvement in the joint properties, laser welding with filler materials has usually been considered too difficult for industrial applications because there are too many parameters and the requirements for wire positioning are too stringent [28], thereby reducing efficiency and productivity. Thus, the possibility to work in autogenous laser keyhole welding is of important technological interest, as it allows a reduction of the time taken in joint preparation and has fewer parameters to control, making it easier to obtain reproducible and stable results [29].

In the present study, an autogenous laser keyhole welding process was introduced to join 6 mm thick steel to Al alloy plates in a butt configuration. The primary objective of this work was to understand the influences of travel speeds and laser beam offsets on the weld shapes, the IMC layers and ultimate tensile strength (UTS) of Al/steel butt joints. Using electron back-scattered diffraction (EBSD) phase mapping, the phase identification and the fracture behavior of IMC layers at the interface were investigated. Based on microstructual and tensile testing, correlations between the processing parameters, IMC layers, and the UTS of Al/steel butt joints were established.

## 2. Materials and Methods

The materials studied in the present work were 6 mm thick 5083 alloy and Q235 low carbon steel plates arranged in a butt configuration, and their nominal compositions are shown in Table 1. Before welding, the oxides on the surface of the aluminum alloy sheet were removed with abrasive paper, and then the surface of the aluminum alloy and steel plates were cleaned with acetone to remove grease and residue. With particular attention to the butt joint, the Al and steel plate edges of the butt joint were also ground, brushed using a stainless steel wire brush, and cleaned thoroughly with ethanol in order to remove the oxide layer in the welding gap.

**Table 1.** Nominal composition of Q235steel and AA5083 alloy (wt %).

| Materials | Si | Mn | S | P | Cr | Ni | Cu | C | Fe | Mg | Zn | Ti | Other | Al |
|---|---|---|---|---|---|---|---|---|---|---|---|---|---|---|
| Q235 | ≤0.35 | 0.3~0.7 | ≤0.045 | ≤0.045 | ≤0.30 | ≤0.30 | ≤0.30 | ≤0.2 | Base | - | - | - | - | - |
| 5083 | ≤0.40 | 0.4~1.0 | | | 0.05~0.25 | | ≤0.10 | | 0.4 | 4.0~4.9 | 0.25 | ≤0.15 | 0.15 | Bal. |

The autogenous laser keyhole welding was carried out by a 6 kW YLR-6000 fiber laser (IPG Photonics, Oxford, MA, USA) with an emission wavelength of 1.07 μm delivering in continuous wave mode through an output fiber core diameter of 100 μm. The laser beam was transmitted through a processing fiber with a diameter of 300 μm, collimated by a lens of 150 mm focal length, and then focused on the materials by a focusing lens with 200 mm focal length. Accordingly, the spot size of focused laser beam was approximately 0.3 mm when the beam-defocused distance was 0 mm. Throughout the experiments, the primary and back-shielding gas, using ultrahigh purity argon gas, was supplied at flow rates of 15 L/min.

The schematic illustration of the welding setup and the principle of laser keyhole-welded Al/steel butt joints is presented in Figure 1. During welding, the focused laser beam was directed onto the steel plate to generate a keyhole, and the solidification of the welding pool formed a weld penetration. Important process parameters for laser keyhole welding affected the weld shapes, including laser power ($P$), travel speed ($v$), defocused distance ($f$), and laser beam offset ($\Delta d$). $P$ and $v$ are generally important process variables affecting the heat input, as in regular arc welding. $\Delta d$ refers to the distance from the laser focus to the interface illustrated in Figure 1b, and is an important parameter only in laser welding, which also controls the welding thermal cycles and cooling rates at the interface [24,30,31]. As a result, the process parameters of $\Delta d$ and $v$ were considered for studying the process parameter influence upon the laser keyhole welded Al/steel butt joints. Thus, $\Delta d$ = 0.3–0.7 mm and $v$ = 0.6–1.2 m/min were varied discretely under the constant conditions of $P$ = 3.25 kW and $f$ = 0 mm.

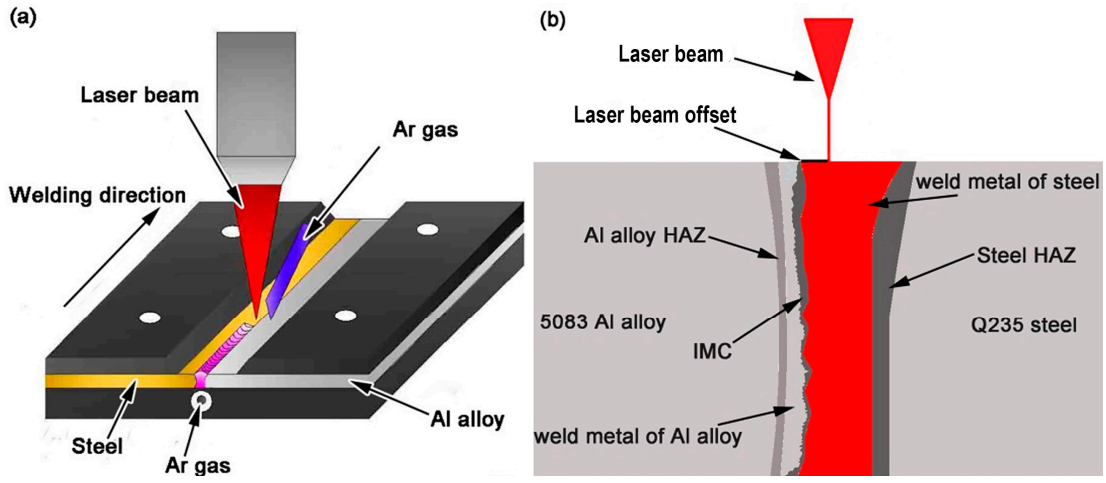


**Figure 1.** Schematic illustration of laser keyhole welding of Al/steel butt joints: (**a**) welding setup; (**b**) principle of laser keyhole welding.

The quality of welded joints is significantly affected by the defects generated in the process of welding dissimilar materials. Thus, after welding, the welding quality was evaluated according to the Chinese welding procedure qualification code DL/T868-2004 and the international standard EN ISO 6520-1 for dissimilar welded joints. An acceptable joint is one in which the weld ripples, the weld width is uniform, and the weld surface should have no visible porosity or hot cracking. Also, there should be no excessive asymmetry or top and root concavity. After the weld surface was checked, X-ray inspection was performed, and the determined quality should be less than grade

II. Then, the acceptable Al/steel butt joints were cut by electro-discharge machining, and this was followed by grinding, polishing and etching. Keller's reagent and Nital acid were used for etching the Al alloys and steels, respectively. The weld appearance and cross-sections were examined using a BX51M optical microscope (Olympus, Tokyo, Japan). The top width ($W_1$) and bottom width ($W_2$) of the weld formed in the steel side, and the area ($S$) of the heat-affected zone (HAZ) formed in the Al alloy side, were used to evaluate the weld shapes of the Al/steel butt joints, as illustrated in Figure 2.

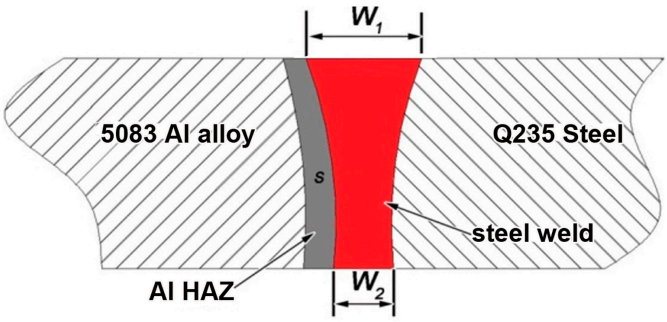


**Figure 2.** Diagram of dimensions of the weld cross section in the Al/steel butt joints.

Vickers microhardness was measured using a HXD-10007 digital and intelligent micro-hardness tester (Caikon, Shanghai, China) with a load of 100 N and 10 s holding time. For each value, the average of five measurements was taken. Uniaxial transverse tensile tests of the Al/steel butt joints were carried out in accordance with the GB/T 228-2002 and GB/T 2651-2001 standards at room temperature using a MTS810 testing machine (MTS, Eden Prairie, MN, USA) operating with a load rate of 1 mm/min. The average UTS value was determined by calculating three tensile specimens.

The IMC layers at the interface of the Al/steel butt joints were preliminarily examined using scanning electron microscopy (SEM, FEI, Hillsboro, OR, USA) with a QUANTA FEG 650 equipped with an energy-dispersive X-ray spectrometer (EDS). Then, EBSD phase mapping was examined in a rectangular zone using a step size of 0.3 μm between two measurements in order to further identify the IMC phases. The EBSD analysis was conducted by a Quanta FEI 650 SEM field emission gun operated at 30 kV and 1.0 nm. The phases and thickness of the IMC layers were analyzed with the HKL-Channel software package (Oxford Instruments, Witney, Oxon, UK). After tensile testing, the failed samples were observed using the SEM and EBSD techniques to study the facture behavior of the IMC layers.

## 3. Results

### *3.1. Weld Appearance of Al/Steel Butt Joints*

Figure 3 shows a representative weld appearance of an Al/steel butt joint under the conditions of $\Delta d$ = 0.6 mm, $v$ = 1.0 m/min, $P$ = 3250 W and $f$ = 0 mm. It is obvious that the top and bottom appearance of the weld are uniform, with regular ripples, except for a little irregularity in proximity to the Al alloys. This means that a relatively acceptable weld appearance of Al/steel butt joints has been achieved by the autogenous laser keyhole-welding process under the optimum welding conditions.

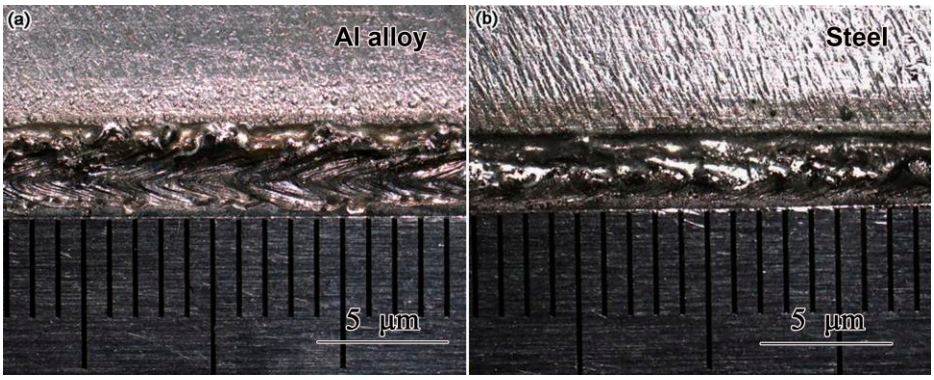


**Figure 3.** Weld appearance of Al/steel butt joints produced by autogenous laser keyhole welding: (**a**) top surface; (**b**) bottom surface.

### *3.2. Cross Sections of Al/Steel Butt Joints*

Figure 4 shows the cross sections of the Al/steel butt joints obtained at different travel speeds under the condition of $\Delta d$ = 0.6 mm, $P$ = 3.25 kW and $f$ = 0 mm. For all the travel speeds, each weld is fully penetrated in keyhole mode. The cross sections of the welds at a travel speed of 0.6 m/min and 0.8 m/min have a "champagne glass" shape, while the weld at 1.0 m/min has a "nail" tape. The welds at 1.1 m/min and 1.2 m/min fall between the two types, with a hybrid of both "nail" and "champagne glass" shapes. Thus, the travel speed plays a major role in forming the weld shape of Al/steel butt joints. In addition, it is obvious that the weld width and weld area decrease rapidly as travel speed increases from 0.6 m/min to 1.0 m/min. At slower travel speeds of 0.6 and 0.8 m/min, a relatively large keyhole weld is generated due to the relatively high welding heat input compared with that of 1.0 m/min. As travel speeds increase from 1.0 to 1.2 m/min, although the amount of time that the laser beam is over a particular zone along the joint is less [32], the resulting level of the top part of the welds increases to some extent, whereas the middle part and bottom part of the welds have a relatively regular interface, resulting in a welding–brazing Al/steel butt joint. Thus, the optimum travel speeds for the best cross section obtained by laser keyhole welding is 1.0 and 1.1 m/min.

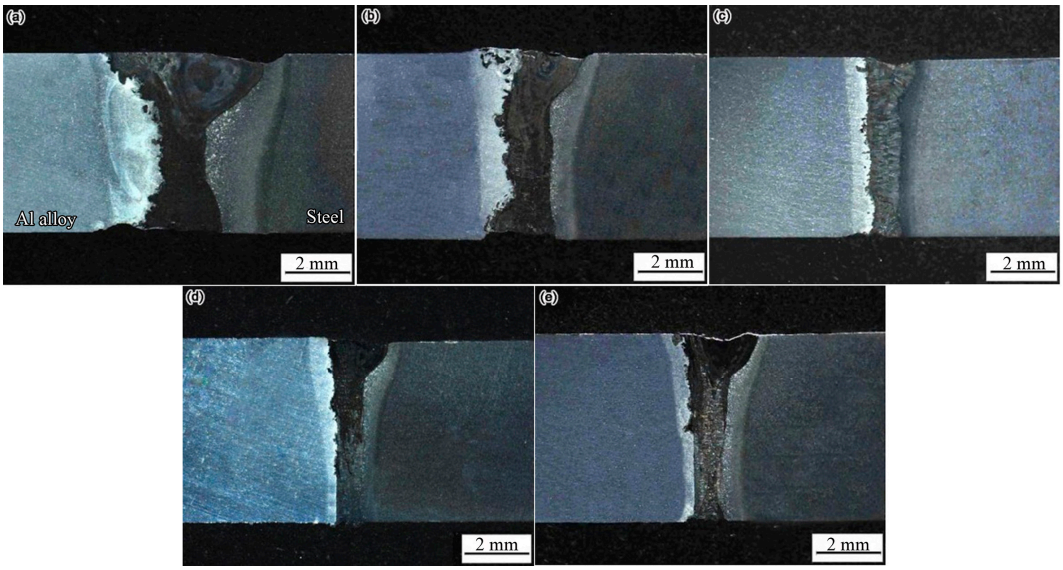


**Figure 4.** Effect of travel speeds on the cross-sections of Al/steel butt joints: (**a**) 0.6 m/min; (**b**) 0.8 m/min; (**c**) 1.0 m/min; (**d**) 1.1 m/min; (**e**) 1.2 m/min.

Figure 5 shows the cross sections of Al/steel butt joints obtained at different laser beam offsets under the condition of $v$ = 1.0 m/min, $P$ = 3.25 kW and $f$ = 0 mm. All the welds possess a similar "nail" type penetration, meaning that the laser beam offsets have no obvious influence on the weld type of Al/steel butt joints. Regarding the weld quality, at relatively low laser beam offsets of 0.3–0.5 mm, the top surfaces of the welds are slightly concave, which is usually caused by excessive metallurgical reactions resulting from the high welding heat input [31]. As the laser beam offset increases to 0.6 and 0.7 mm, the concavity of the welds is considerably reduced due to the decrease of the heat input. In addition, at relatively low laser beam offsets of 0.3–0.4 mm, the interface boundary is seriously uneven along the joint thickness because of the excessive metallurgical reactions happening at the interface. When the laser beam offsets continuously increase to 0.6 and 0.7 mm, the excessive metallurgical reaction of the interface is lessened. As a result, the acceptable laser beam offsets for laser keyhole welding of Al/steel butt joints is 0.6 and 0.7 mm.

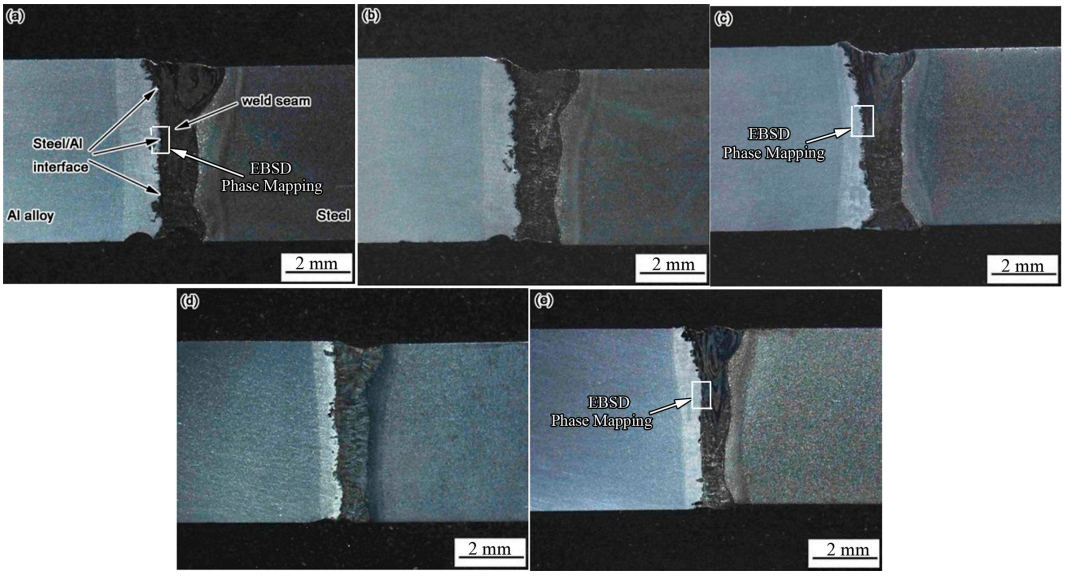


**Figure 5.** Effect of laser beam offsets on the cross-sections of Al/steel butt joints: (**a**) 0.3 mm; (**b**) 0.4 mm; (**c**) 0.5 mm; (**d**) 0.6 mm; (**e**) 0.7 mm.

However, the thermal cycle suffered at the interface from the top to the bottom of the joints is different, because laser welding has a high temperature gradient of through-thickness, which induces uneven distribution of reaction layer morphology, leading to different reaction modes. At the top part of the steel/Al alloy joints, the interface generated an excessive metallurgical reaction showing fusion joint characteristics as a result of the relatively high heat input. However, in some regions of the interface, such as in the middle part, or the one close to the bottom, a relatively regular interface line due to the reduced heat input is revealed. It is found that a narrow zone of solid steel HAZ is formed between the fusion weld and the Al alloy, and the interfacial reaction mode is transformed from fusion-melting to brazing, which proves that a welding–brazing butt joint has been obtained by the keyhole laser welding process.

The effects of travel speeds and laser offsets on $W_1$, $W_2$, $S$ are illustrated in Figure 6. As shown in Figure 6a, $S$ decreases sharply from 6.84 to 3.42 mm$^2$ with the increase of travel speeds from 0.6 to 1.0 m/min, and decreases slowly from 2.76 to 2.10 mm$^2$ with increasing travel speeds from 1.1 to 1.2 m/min; indicating that $S$ is decreased continuously with increasing travel speeds from 0.6 to 1.2 m/min. The decrease of $S$ is due to the fact that the laser beam interacts with the steels for a shorter period of time as travel speed increases [33], and thus less molten weld metal is produced, causing $S$ to decrease continuously. As shown in Figure 6b, the $S$ decreases sharply from 4.56 to 2.64 mm$^2$, and then decreases slowly from 2.22 to 1.92 mm$^2$ with increasing laser offsets from 0.3 to 0.7 mm. The decrease

of *S* with increasing laser beam offsets is due to the fact that the heat input at the interface is decreased continuously with increasing laser beam offsets [9]. This indicates that the travel speeds and laser beam offsets directly impact the molten zone of the Al alloy side, which contributes to the final weld quality of the interface.

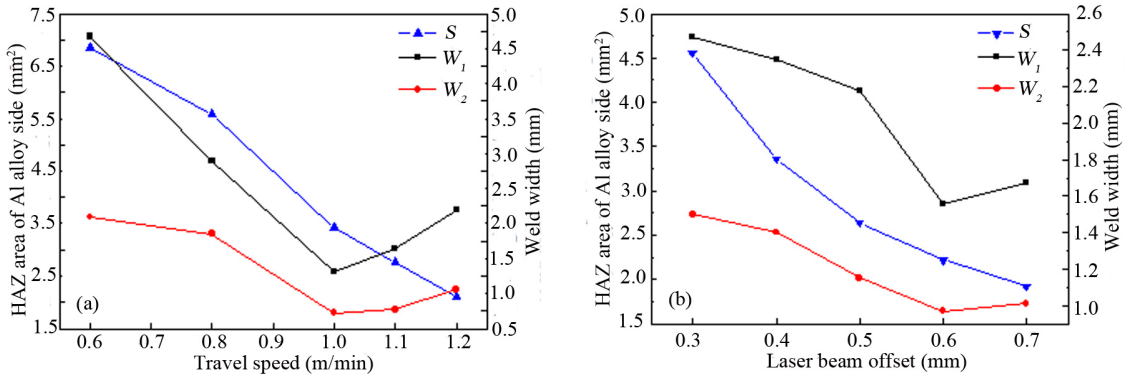


**Figure 6.** Relationship between process parameters and weld width or the heat-affected zone (HAZ) of the Al side: (**a**) travel speeds; (**b**) laser beam offsets. Blue color corresponds to HAZ; Black and red color correspond to top width ($W_1$) and bottom width ($W_2$) of the welds.

Concerning the weld width, the $W_1$ decreases sharply from 4.92 to 1.56 mm, and then increases slowly from 1.81 to 2.44 mm, as travel speed increases from 0.6 to 1.2 m/min. The $W_2$ decreases gradually from 2.34 to 0.97 mm with the increase of travel speeds from 0.6 to 1.0 m/min, and then increases a little from 1.02 to 1.31 mm with the increase of travel speeds from 1.0 to 1.2 m/min. This indicates that travel speed has a significant effect on $W_1$, but has less influence on $W_2$. In the case of laser beam offsets, $W_1$ decreases gradually from 2.47 to 1.67 mm and $W_2$ decreases a little from 1.5 to 1.0 mm, as the laser beam offsets increase from 0.3 to 0.7 mm, indicating that a varying laser beam offset influences $W_1$ and $W_2$ somewhat. Consequently, varying travel speeds and laser beam offsets have a more pronounced effect on *S* than on weld width.

### *3.3. Microstructures of Al/Steel Joint*

The typical cross section of an Al/steel joint with a laser beam offset 0.3 mm was observed and analyzed. Several different zones shown in Figure 7a and the characteristics of each are discussed in detail. Figure 7b,d,f presents an enlarged view of zones A, B and C as shown in Figure 7a. Figure 7b shows the microstructure of the steel-fusion zone, steel HAZ and steel base metal, showing the variation of grain morphology along with the decline of heat input. Figure 7c,e shows high-magnification microstructures of steel fusion and steel HAZ, corresponding to zones marked by white dashes and red dashes shown in Figure 7b, respectively. It can be noticed that the steel-fusion zone has a coarser lath structure, which contains martensite microstructures after rapid cooling, while the steel HAZ consists of granular bainite. Figure 7d shows an enlarged view of zone B shown in Figure 7a, and displays the typical microstructure of a steel seam which is mainly composed of columnar crystal. Grain size is from 100 to 200 μm. Moreover, columnar crystal was nearly perpendicular to the fusion boundary, which is induced by the higher cooling rate in this direction and the characteristic of the preferred growth of crystallized grains [24].

Figure 7f displays an enlarged view of zone C shown in Figure 7a, revealing the microstructure of the Al side of the Al/steel joint. It can be seen that the welding joint is formed between the molten aluminum weld metal and local molten steel. IMC layers were produced along the Al/steel interface, with broken IMC phases in the neighboring Al alloy weld metal. In this area, the changes of grain size can be observed, which may confirm the fact that heat input affects the process of crystallization and growth. Figure 7g shows the Al fusion zone marked by white dashes in Figure 7f. The microstructure

of the base metal is very different to that of the fusion zone. The external Al fusion zones close to the base metal (shown in Figure 7g), are characterized by dendritic growth, which corresponds to the zones with higher solidification rates [34].

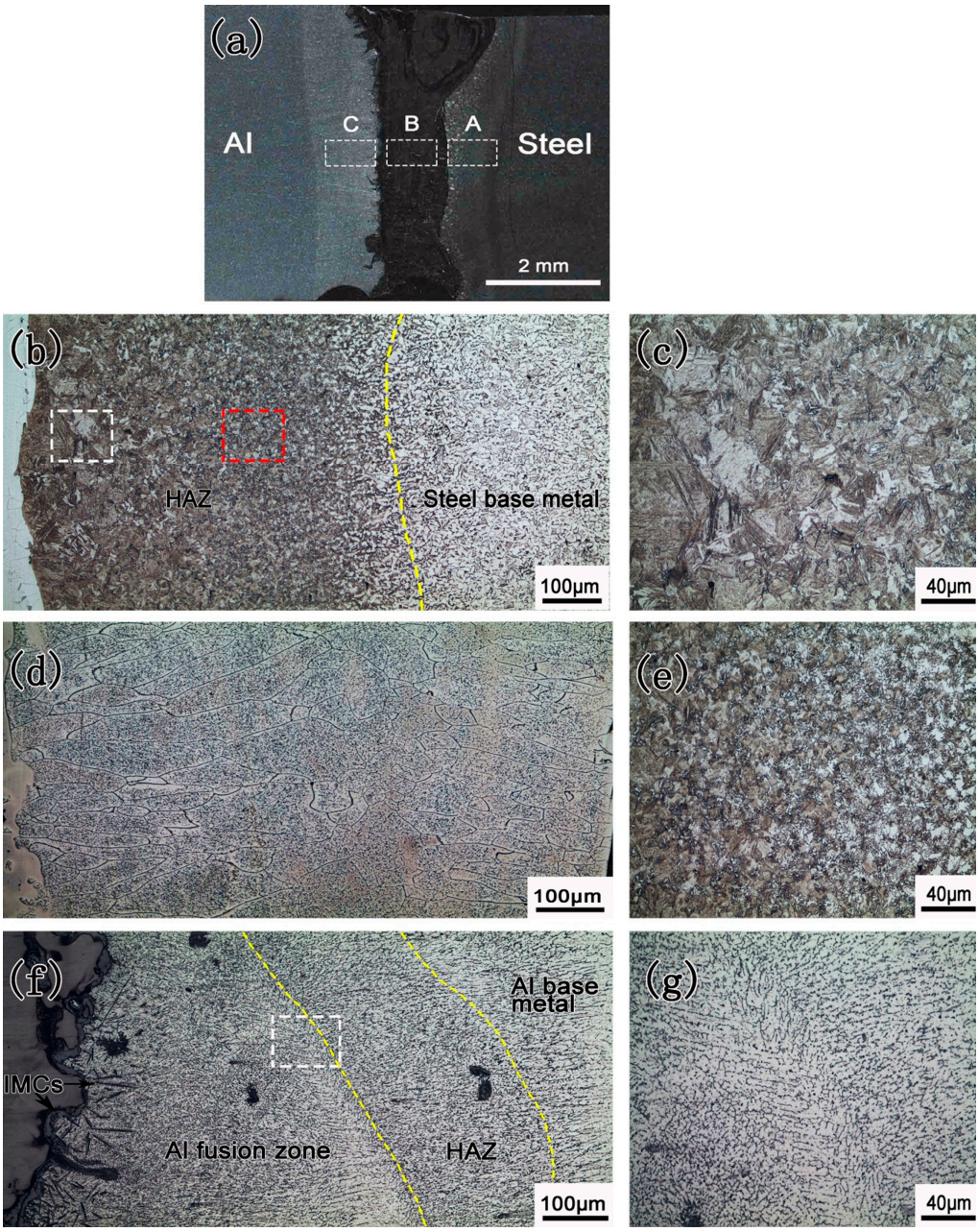


**Figure 7.** Cross-section microstructure of laser welding–brazing joint of aluminum and steel: (**a**) cross section of joint; (**b**) enlarged zone A in (**a**); (**c**) enlarged zone marked by white dashes in (**b**); (**d**) enlarged zone B in (**a**); (**e**) enlarged zone marked by red dashes in (**b**); (**f**) enlarged zone C in (**a**); (**g**) enlarged zone marked by white dashes in (**f**).

### *3.4. Phase Identification of Intermetallic Compound (IMC) Layers*

Figure 8 shows a back-scattered scanning electron (BSE) micrograph of a thick IMC layer at the interface of Al/steel butt joints produced under the same conditions of $\Delta d$ = 0.4 mm, $P$ = 3.25 kW, $f$ = 0 mm and $v$ = 1.0 m/min. It was found that the IMC layers were composed of a large needle-like phase ("1") dispersed in the Al alloy side, a compact lath structure ("2") having a relatively smooth

boundary adjacent to the steel side, and a fine serrated phase ("3") grown from the "2" layer. An elemental composition analysis from EDS was conducted on the location "1", "2" and "3", and the results are shown in Figure 8. The composition of location "1" is 77.09 at % Al and 22.91 at % Fe, which is similar to that of location "3", and the one for location "2" is 72.81 at % Al and 27.19 at % Fe. Compared to the measured composition with the Fe–Al phase diagram, the compositions of location "1" and "3" are in accordance with $FeAl_3$, and the location "2" can be the $Fe_2Al_5$ phase. Therefore, EDS analysis shows that the IMC layers at the interface consists of $FeAl_3$ and $Fe_2Al_5$ phases. Concerning the formation sequence and phase growth, some references have shown that the $Fe_2Al_5$ would be formed first. An indication that the $Fe_2Al_5$ is the phase that is formed first is its wavy interface towards the $FeAl_3$, which indicates in a binary system that it was a former interface between a liquid and a solid, while the straight interface of the $Fe_2Al_5$ on the steel side indicates solid-state diffusion [35]. A further indication of the prior formation of the $Fe_2Al_5$ is the fact that each $Fe_2Al_5$ grain is a direct neighbor of several $FeAl_3$ grains, thus it appears likely that the $FeAl_3$ nucleated at the interface of the already formed $Fe_2Al_5$ [36].

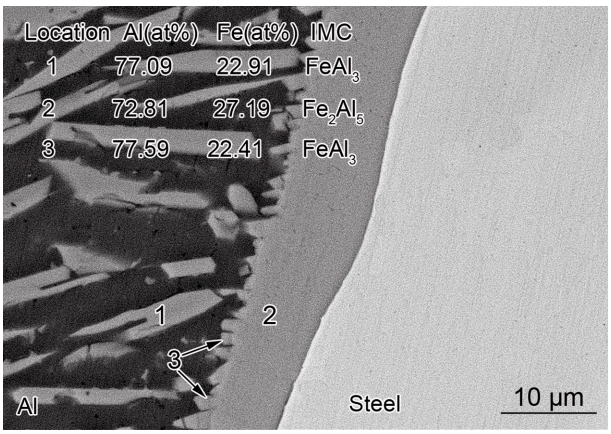


**Figure 8.** Back-scattered scanning electron (BSE) micrograph and energy dispersive spectrometry (EDS) analysis result of intermetallic compound (IMC) layers at the interface.

An interface region including the Al alloy, IMC layers and steel base metal was measured using EBSD phase mapping to obtain statistically significant phase information formed at the steel/Al alloy butt joints, as shown in Figure 9. The phase type of the IMC layers was accurately determined by Kikuchi patterns and the lattice constants using EBSD phase mapping performed at a selected rectangular zone near the middle part (plotted in Figure 5) of the Al/steel butt joints. The colors in phase mapping is based on a color-coded legend, in which the red, yellow, blue and green correspond to the α-Fe, α-Al, $Fe_2Al_5$, and $Fe_4Al_{13}$ phases, respectively. As shown in Table 2, the $Fe_4Al_{13}$ phase had a monoclinic unit cell with $a$ = 15.49 Å, $b$ = 8.08 Å, $c$ = 12.48 Å, and β = 107.72°, and the $Fe_2Al_5$ phase had an orthorhombic crystal with lattice constants of $a$ = 7.66 Å, $b$ = 6.42 Å, $c$ = 4.22 Å, and β = 90°, which is consistent with that of the previous studies [25,37]. Note that the $Fe_4Al_{13}$ phase here was the same as the equilibrium $FeAl_3$ phase identified by preliminary EDS analysis. Figure 8 displays EBSD phase mapping of the IMC layers at the interface for the Al/steel butt joints obtained at a laser beam offset of 0.3 mm. According to Table 2 and Figure 8, the needle-like, serrated $Fe_4Al_{13}$ phase and lath $Fe_2Al_5$ phases were formed at the interface, which agrees with the early results obtained by Dybkov [38] and Shi et al. [37]. They have proposed that the reaction products are a solid solution based upon the $Fe_4Al_{13}$ and $Fe_2Al_5$ [15]. Therefore, by EDS and EBSD analysis, it can be confirmed that the IMC layers at the interface were composed of $Fe_4Al_{13}$ and $Fe_2Al_5$ phases.

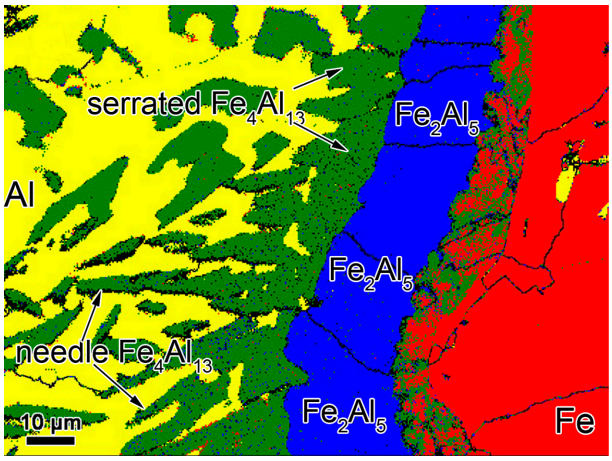


**Figure 9.** EBSD phase mappings of the interface of Al/steel joints at a laser beam offset of 0.3 mm.

**Table 2.** Intermetallic compound (IMC) phases identified using electron back-scattered diffraction (EBSD) phase mapping.

| Symbol | Phase | *a* | *b* | *c* | Alpha | Beta | Gamma | Space Group |
|---|---|---|---|---|---|---|---|---|
| θ | $Fe_4Al_{13}$ | 15.49 Å | 8.08 Å | 12.48 Å | 90.00° | 107.72° | 90.00° | 12 |
| η | $Fe_2Al_5$ | 7.66 Å | 6.42 Å | 4.22 Å | 90.00° | 90.00° | 90.00° | 63 |

### *3.5. Morphology and Thickness of IMC Layers*

Figure 10 shows the BSE micrographs of the IMC layers at the interface of the Al/steel butt joints with different travel speeds. At a travel speed of 0.6 m/min, the IMC morphology formed at the interface exhibits a number of large needle-like $FeAl_3$ phases and thick $Fe_2Al_5$ layers owing to the high heat input induced by the slow travel speeds. With the increase of travel speeds from 0.8 to 1.2 m/min, the quantity of large needle-like $FeAl_3$ phases was significantly decreased and the thickness of the $Fe_2Al_5$ layers was also reduced. In particular, the large needle-like $FeAl_3$ phases dispersed in the Al alloy completely disappeared when the travel speed was increased from 1.0 m/min to 1.2 m/min. The effect of the travel speeds on the quantity of the needle-like $FeAl_3$ may be attributed to the decrease of the cooling rate of the interface [11]. Figure 10f displays the thickness of the IMC layers as a function of travel speeds. Here, the thickness of $Fe_2Al_5$ layers is used to evaluate the IMC layer because of its regularity. The thickness of $Fe_2Al_5$ layers decreased sharply from 47.7 to 15.1 μm from 0.6 to 0.8 m/min, and then decreased slowly from 7.9 to 4.7 μm with the increase of travel speeds from 1.0 to 1.2 m/min. The decrease of $Fe_2Al_5$ layer thickness at the interface can be explained by the reduction of linear energy input with the increase of travel speeds [33].

The IMC layers at the interface of the Al/steel butt joints with different laser beam offsets are shown in Figure 11. At relatively low laser beam offsets of 0.3–0.5 mm, it was obvious that a great number of large needle-like $FeAl_3$ phases and thick $Fe_2Al_5$ layers were formed at the interface. With increasing laser beam offsets from 0.6 to 0.7 mm, the quantity of large needle-like $FeAl_3$ phases dispersed in the Al alloy significantly decreased, and only compact lath $Fe_2Al_5$ layer and fine serrated $FeAl_3$ phases attached to $Fe_2Al_5$ layer were observed at the interface. Therefore, that laser beam offset decreases greatly the quantity of large needle-like $FeAl_3$ phases at the interface. Concerning the effect of laser beam offsets on the IMC layer thickness, it was found that the thickness of $Fe_2Al_5$ layers decreased quickly from 21.0 to 9.6 μm with the increase of laser beam offsets from 0.3 to 0.4 mm, and then decreased gradually from 7.8 to 4.1 μm as laser beam offsets increase from 0.5 to 0.7 mm, as shown in Figure 11f. The decrease of the $Fe_2Al_5$ layer thickness with the increase of laser beam offsets was mainly caused by the decrease in the maximum temperature and the reaction time at the interface [30,39]. With the increase of the laser offsets, the maximum temperature at the interface

tends to be lower and the time for diffusion and dissolution of Fe atoms decreases, giving a thinner IMC layer.

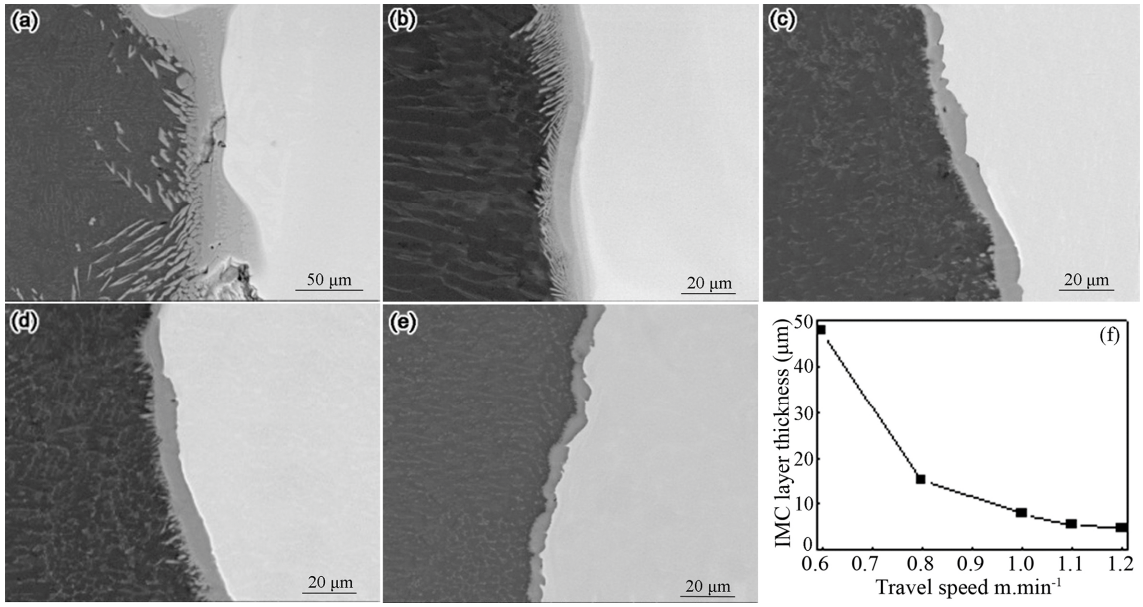


**Figure 10.** IMC layer microstructures at the interface of the Al/steel butt joints with different travel speeds: (**a**) 0.6 m/min; (**b**) 0.8 m/min; (**c**) 1.0 m/min; (**d**) 1.1 m/min; (**e**) 1.2 m/min; (**f**) thickness of the IMC layers (contained in the second panel).

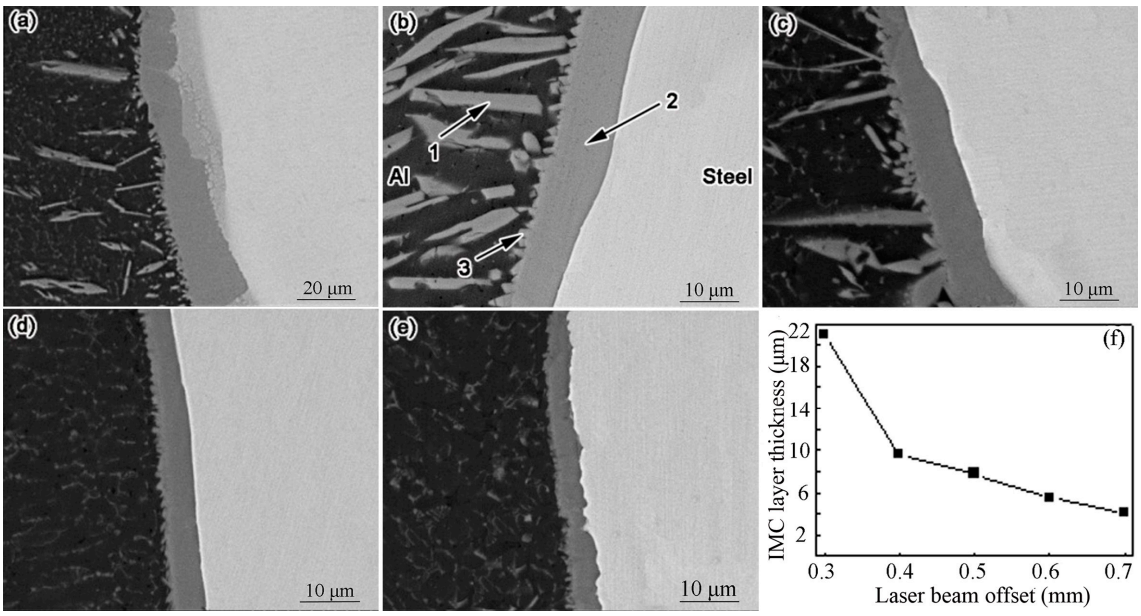


**Figure 11.** IMC layer microstructures at the interface of the Al/steel butt joints with different laser beam offsets: (**a**) 0.3 mm; (**b**) 0.4 mm; (**c**) 0.5 mm; (**d**) 0.6 mm; (**e**) 0.7 mm; (**f**) thickness of IMC layers.

### *3.6. Microhardness Profile of Al/Steel Butt Joints*

Figure 12 shows the microhardness distribution of the Al/steel butt joints with different laser beam offsets. It was found that the average microhardness of 5083 Al alloys and Q235 steels is 74.1 and 142.3 HV, while the weld and HAZ microhardness at the steel side reach 258.4 and 185.5 HV, respectively. The higher hardness in the weld is mainly caused by the steel hardening because of the

quenching effect, and the high hardness in the HAZ is related to the high heating and cooling rate experienced in the HAZ resulting in a fine microstructure [40].

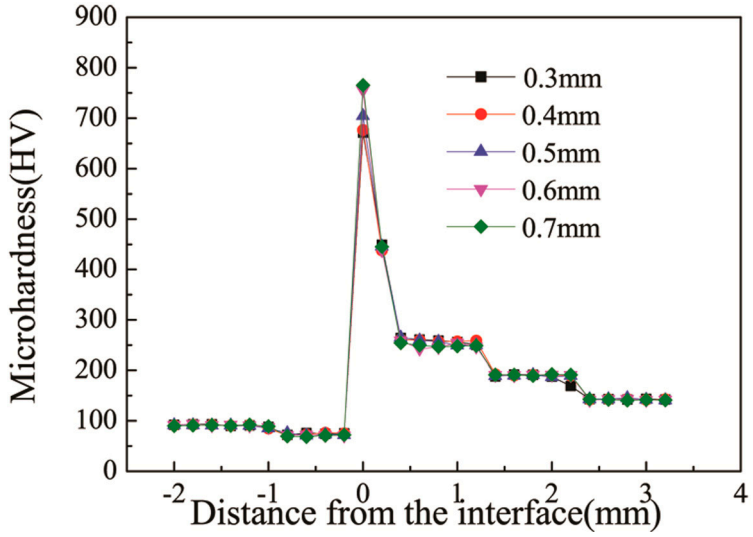


**Figure 12.** Microhardness distribution in the Al/steel butt joints.

The hardness at the interface of the Al/steel butt joints increased abruptly in the range from 600 to 800 HV from the laser beam offset of 0.3 to 0.7 mm, as seen in Figure 11a. The higher hardness at the interface was due to the presence of the brittle $Fe_2Al_5$ and $Fe_4Al_{13}$ phases [13]. In addition, the lowest hardness of 0.3 mm was 671.3 HV, and the highest hardness was 765.4 HV for the laser beam offset of 0.7 mm. The difference in hardness at the interface between the laser beam offsets of 0.3 mm and 0.7 mm was closely associated with the different morphology of the IMC layers generated at the interface. As mentioned above, at a laser beam offset of 0.3 mm, the IMC layers at the interface were composed of a thick lath $Fe_2Al_5$ layer, large needle-like and fine serrated $Fe_4Al_{13}$ phases, due to the excessive reactions at the interface as a result of the high heat input caused by a small laser beam offset of 0.3 mm. However, at a relatively higher laser beam offset of 0.7 mm, the IMC layers at the interface consisted of only thin lath $Fe_2Al_5$ layer and fine serrated $Fe_4Al_{13}$ phases as a result of the lesser heat input. Thus, at the laser beam offset of 0.7 mm, the hardness at the interface mainly depended on $Fe_2Al_5$ layers, which have a higher hardness than $Fe_4Al_{13}$ layers [41]. This explained why the joint with a laser beam offset of 0.7 mm had the higher hardness at the interface.

### *3.7. Tensile Properties of the Al/Steel Butt Joints*

The UTS of the Al/steel butt joints was influenced significantly by travel speeds and laser beam offsets, as shown in Figure 13. Figure 13a shows the UTS of the Al/steel butt joints increased rapidly from 64.0 to 110.4 MPa with the increase of travel speeds from 0.6 to 1.0 m/min, and then decreased to 77.3 MPa at the travel speed of 1.2 m/min, which indicates that the UTS of the Al/steel butt joints reached its maximum at the travel speed of 1.0 m/min. It can be seen from Figure 13b that the UTS of the Al/steel butt joints was increased from 42.0 to 107.0 MPa by increasing laser beam offsets from 0.3 to 0.6 mm, while the UTS of the Al/steel butt joints decreased to 96.0 MPa as laser beam offset continuously increased to 0.7 mm. Thus, the maximum UTS of 107.0 MPa was obtained at a laser beam offset of 0.6 mm. Consequently, the UTS of the Al/steel butt joints reached its maximum in the conditions of a laser beam offset of 0.6 mm or a travel speed of 1.0 m/min.

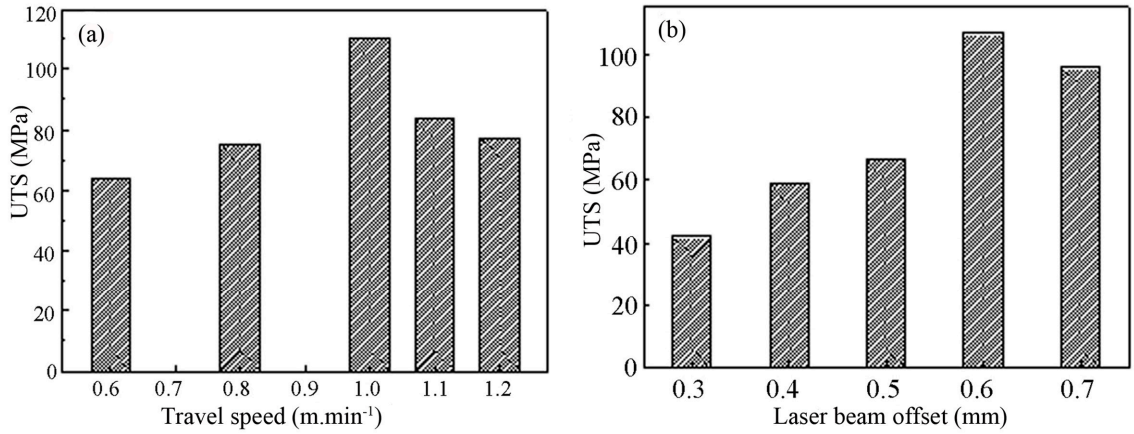


**Figure 13.** Effect of laser-welding parameters on the ultimate tensile strength (UTS) of the Al/steel butt joints: (**a**) travel speeds; (**b**) laser beam offsets.

The relatively low UTS of Al/steel butt joints is primarily due to the formation of brittle IMC phases at the interface, which is the main cause of embrittlement [42]. All the Al/steel butt joints failed at the IMC layers at the interface, as shown in Figure 14. During the tensile test, the crack firstly initiated at the top part ("I" zone in Figure 14a) or the bottom part ("III" zone in Figure 14c) of the IMC layers. Finally, it propagated into the middle part ("II" zone in Figure 14b) of the IMC layer, which led to the failure of the Al/steel butt joint. The fracture occurring at the IMC layer was related to the brittleness and morphology of the IMC layers at the interface. At the top part of the IMC layer, a thick $Fe_2Al_5$ layer and a number of the large needle-like $Fe_4Al_{13}$ phases were observed owing to the high heat input. For the bottom part of the IMC layer, some welding undercuts were observed at the root of the joint in the Al alloy side close to the interface, which was more inclined to initiate microcracks at high loads during the tensile test. Therefore, it can be supposed that the crack starts from the bottom or top part, and propagates into the middle part of the IMC layer at the interface.

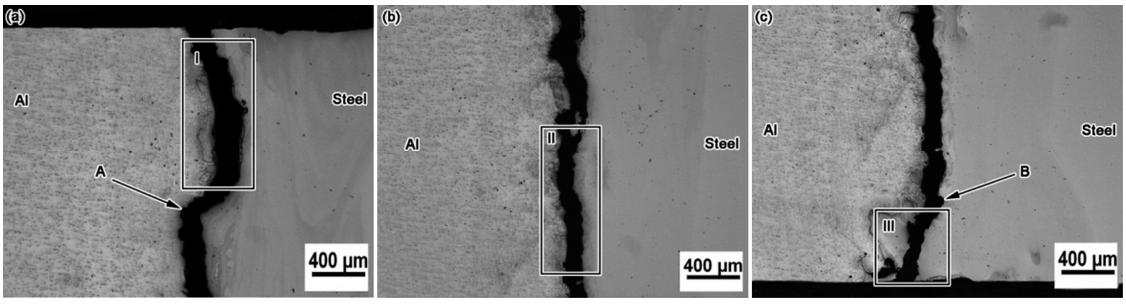


**Figure 14.** Fracture path of the interface at the steel/Al alloy butt joint: (**a**) top position (**b**) middle position (**c**) bottom position.

Figure 15 shows typical results from SEM investigations of fracture surfaces at the steel side and Al alloy side of the position "II" in the Al/steel butt joints, as this region is the final failure location of the joint during tensile tests. The fracture surface at the Al alloy side can be seen to be mostly flat, and the microcrack grows through the grains. Also, there was evidence of some broken $Fe_4Al_{13}$ phases and the needle-like $Fe_2Al_5$, as shown in Figure 15a, which depicts brittle transgranular fracture. The factographic surface in the steel side shown in Figure 15b presented the typical cleavage fracture mode, with river pattern strips of particular orientation on the fracture surface, which occupies the largest fraction area of the sample surface exhibiting interfacial failure. Even though the failure of all the samples was always located at the brazing interface during the tensile test, the specimens endured

some plastic deformation, as shown in Figure 15c; some regions of the factographic surface in the steel side appear to show some dimples accompanied by some local plasticity, and the crack grew along the grain boundary, showing some intergranular fracture characteristics. Although these fractures were brittle, the latter had a certain resistance to the crack propagation of the IMC layers at the steel side, which enhanced its mechanical resistance at the steel side. As a result, the IMC layer region close to the Al base material was the most brittle region having the weakest bonding strength at the interface.

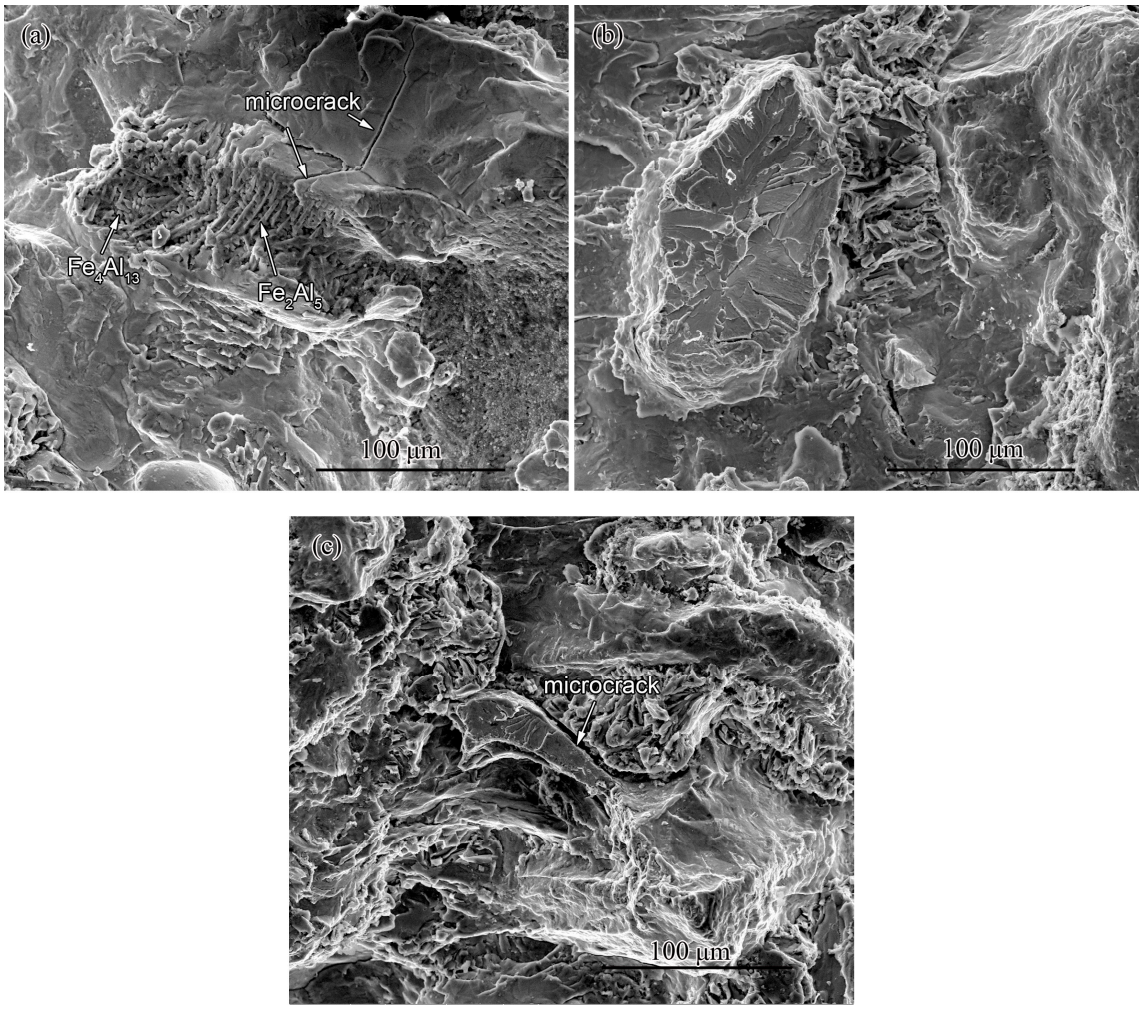


**Figure 15.** Scanning electronic microscope (SEM) micrographs of the middle position at the interface of the steel/Al alloy butt joint: (**a**) Al alloy side; (**b**) steel side; (**c**) steel side showing some dimples.

## 4. Discussion

### *4.1. Effect of IMC Layer Thickness on Ultimate Tensile Strength (UTS)*

The relationship between the IMC layer thickness and the UTS of Al/steel joints has been proposed by Borrisutthekul [12], showing that the UTS was increased with decreasing thickness of the reaction layer. In the present study, increasing travel speeds from 0.6 to 1.0 m/min improved the UTS of Al/steel joints, as shown in Figure 13a, due to the decreased thickness of the IMC layer continuously from 47.7 to 7.9 μm (Figure 10f). In Figure 13b, with the increase of laser beam offsets from 0.3 to 0.6 mm, the UTS of Al/steel joints was increased as the IMC layer thickness decreased from 21.0 to 5.6 μm (Figure 11f). In these cases, the increased tendency of the UTS with decreasing IMC layer thickness was clearly observed, which is in good agreement with the results reported by Borrisutthekul [12].

However, with continuously increasing travel speeds to 1.2 m/min or increasing laser beam offset to 0.7 mm, the UTS of the Al/steel joints was not increased continuously with further reductions in IMC layer thickness. This indicates that the UTS of Al/steel joints does not always increase with a decrease in IMC layer thickness [3]. Gao et al. [17] has proposed that there is an optimal range of IMC layer thickness for improving the UTS of Al/steel joints, because an IMC layer that is too thin or too thick results in low UTS. The reasons are due to the fact that an IMC layer that is too thin means an insufficient interface reaction leads to the lack of fusion, and the IMC layer that is too thick resulting from an excessive growth of the IMC phases increased the interface brittleness [17]. Therefore, it is concluded that there is a relationship between optimum IMC layer thickness and the UTS of Al/steel butt joints. However, this is not the sole condition. When comparing the thickness of the IMC layer of the joints welded with a welding speed of 0.6 m/min and those welded with a laser offset of 0.5 mm, it is found that the thickness for a welding speed of 0.6 m/min is about ~48 μm, and the joint has a low UTS of 64.0 MPa. For a laser beam offset of 0.5 mm, the IMC layers have thin thickness of 7.8 μm, whereas the joints also exhibit low UTS of 66.5 MPa. Therefore, for thickness of more than 10 μm, the increased tendency of UTS with decreasing IMC layer thickness is clearly observed, which is in good agreement with the results reported by Borrisutthekul [12]. However, with continuously decreasing thickness to less than 10 μm, the UTS of Al/steel joints not only largely depends on the IMC layer thickness, but also on the IMC phase type and morphology at the interface.

### *4.2. Fracture Behavior of IMC Layers*

It is well accepted that the UTS of Al/steel joints largely depends on the IMC layers (thickness and phase type) at the interface [43]. However, regarding the fracture behavior of IMC layers during tensile processing, there are some contradictory results. Springer et al. pointed out that the crack propagated in the brittle IMC phases and cut through the remainder of the steel at the irregular, wavy steel/$Fe_2Al_5$ interface [44]. However, Chen et al. claimed that the $Fe_2Al_5$ layer was the primary and most brittle phase at the interface [43]. These observations are evidence that the fracture of IMC layers associated with tensile testing are not well understood. Thus, in the present study, an EBSD phase mapping of the fractured surfaces of Al/steel butt joints under three laser beam offsets was conducted in order to understand the fracture behavior of the IMC layers at the interface. At a laser beam offset of 0.3 mm, it is evident that the crack travels through $Fe_2Al_5$ layers and the fracture path is smooth, as shown in Figure 16a, while the $Fe_4Al_{13}$/$Fe_2Al_5$ and $Fe_2Al_5$/steel phase interface bond well. This indicates that the $Fe_2Al_5$ layer is the weakest in terms of bonding strength of the IMC layers at the interface, and a transgranular fracture that occurred at the $Fe_2Al_5$ layers is evident due to the higher hardness of the $Fe_2Al_5$ layers [41] (Figure 12). Figure 16b shows a brittle transgranular fracture still occurring at $Fe_2Al_5$ layer at a laser beam offset of 0.5 mm, but some second cracks can be observed in the Al base material, showing that some deformation has happened at the interface. This explains why the Al/steel butt joint at a laser beam offset of 0.5 mm has relatively high UTS compared to that of a laser beam offset of 0.3 mm. When the laser beam offset is 0.7 mm (Figure 16c), it clearly reveals that the crack travels along the boundary of the $Fe_2Al_5$ grains and the fracture path shows the obvious irregularity, which demonstrates evidence that an intergranular fracture occurred at the $Fe_2Al_5$ layers. Thus, the intergranular fracture occurring at the $Fe_2Al_5$ layer is thought to be attributable to the relatively high UTS of the Al/steel butt joints with a laser beam offset of 0.7 mm. Consequently, the present study of EBSD phase mapping shows that the $Fe_2Al_5$ layer is the most brittle region having the weakest bonding strength, which is entirely consistent with a previous study reported by Chen et al. [43]. Moreover, an intergranular fracture that occurred at the $Fe_2Al_5$ layers led to a relatively high UTS of the Al/steel butt joints.

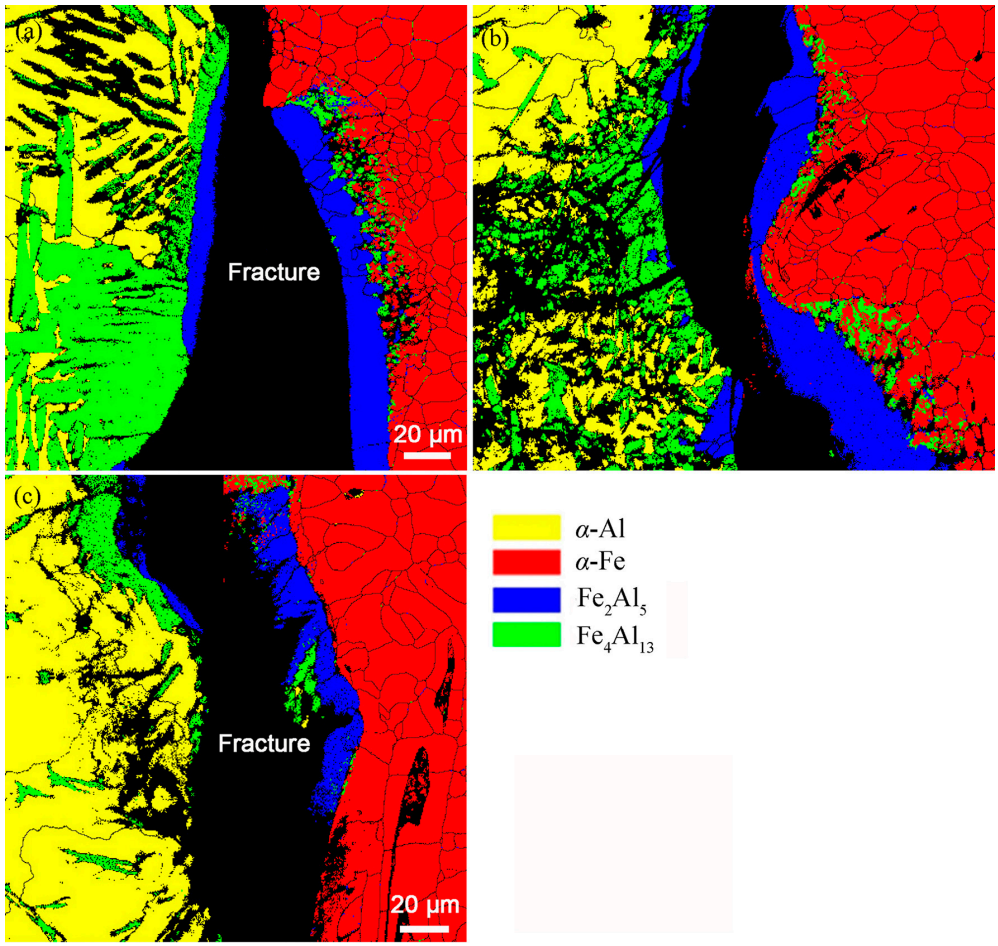


**Figure 16.** EBSD phase mapping of the failed tensile samples for the Al/steel joint with different laser beam offsets: (**a**) 0.3 mm; (**b**) 0.5 mm; (**c**) 0.7 mm.

## 5. Conclusions

Based on the above results and discussion, butt joints of 6.0 mm thick 5083 Al alloys to Q235 steel plates have been achieved by using autogenous laser keyhole welding. The following conclusions can be drawn from this work:

(1) Varying travel speeds and laser beam offsets have a more pronounced effect on the area of HAZ *S* than on weld width. By increasing the laser beam offsets and welding speed, the *S* in the Al alloy side is decreased continuously. However, travel speed has a significant effect on $W_1$, but has less influence on $W_2$, whereas varying laser beam offset influences $W_1$ and $W_2$ a little.

(2) The thickness of $Fe_2Al_5$ layers decreases from 47.7 to 4.7 μm with increasing travel speeds from 0.6 to 1.2 m/min. As laser beam offset increases from 0.3 to 0.7 mm, the thickness of $Fe_2Al_5$ layers decreases from 21.0 to 4.1μm. Thus, increasing travel speeds or laser beam offsets obviously decreases the quantity of long needle-like $FeAl_3$ phases and the thickness of the $Fe_2Al_5$ layer.

(3) The UTS of Al/steel butt joints is influenced significantly by the tested travel speeds and laser beam offsets. The UTS reaches its maximum under the conditions of a travel speed of 1.0 m/min or a laser beam offset of 0.6 mm. There should be a matching relationship between the IMC layer thickness and UTS of Al/steel butt joints.

(4) EBSD phase mapping proves that the IMC layers consist of $Fe_2Al_5$ phases and $Fe_4Al_{13}$ phases. Increasing laser beam offsets from 0.3 to 0.7 mm significantly decreases the quantity of $Fe_4Al_{13}$ phases and the thickness of $Fe_2Al_5$ layers at the interface of Al/steel butt joints.

(5) EBSD phase mapping proves that the $Fe_2Al_5$ layer is the most brittle region having the weakest bonding strength. An intergranular fracture occurring at the $Fe_2Al_5$ layers leads to the relatively high UTS of Al/steel butt joints.

**Acknowledgments:** This work was supported by the National Natural Science Foundation of China (grant number 51475006) and the Key Program of Science and Technology Projects of Beijing Municipal Commission of Education (grant number KZ201610005004). The authors are grateful to Steve Shi from TWI Ltd. (Cambridge, UK) for providing language help and editing this manuscript.

**Author Contributions:** Li Cui and Dingyong He conceived and designed the experiments; Wei Qian performed the welding experiments; Boxu Chen analyzed the data; Li Chen contributed analysis tools; Li Cui wrote the paper.

**Conflicts of Interest:** The authors declare no conflict of interest.

## References

1. Thomy, C.; Vollertsen, F. Laser-MIG hybrid welding of aluminium to steel—Effect of process parameters on joint properties. *Weld. World* **2012**, *56*, 124–132. [CrossRef]
2. Qin, G.; Lei, Z.; Su, Y.; Fu, B.; Meng, X.; Lin, S. Large spot laser assisted gma brazing–fusion welding of aluminum alloy to galvanized steel. *J. Mater. Process. Technol.* **2014**, *214*, 2684–2692. [CrossRef]
3. Mathieu, A.; Shabadi, R.; Deschamps, A.; Suery, M.; Matteï, S.; Grevey, D.; Cicala, E. Dissimilar material joining using laser (aluminum to steel using zinc-based filler wire). *Opt. Laser Technol.* **2007**, *39*, 652–661. [CrossRef]
4. Meco, S.; Pardal, G.; Ganguly, S.; Williams, S.; Mcpherson, N. Application of laser in seam welding of dissimilar steel to aluminium joints for thick structural components. *Opt. Laser Eng.* **2015**, *67*, 22–30. [CrossRef]
5. Tricarico, L.; Spina, R. Experimental investigation of laser beam welding of explosion-welded steel/aluminum structural transition joints. *Mater. Des.* **2010**, *31*, 1981–1992. [CrossRef]
6. Lahdo, R.; Springer, A.; Pfeifer, R.; Stefan, K.; Ludger, O. High-power laser welding of thick steel-aluminum dissimilar joints. *Phys. Procedia* **2016**, *83*, 396–405. [CrossRef]
7. Atabaki, M.M.; Ma, J.; Liu, W.; Kovacevic, R. Hybrid laser/arc welding of advanced high strength steel to aluminum alloy by using structural transition insert. *Mater. Des.* **2015**, *75*, 120–135. [CrossRef]
8. Song, J.L.; Lin, S.B.; Yang, C.L.; Ma, G.C.; Liu, H. Spreading behavior and microstructure characteristics of dissimilar metals tig welding–brazing of aluminum alloy to stainless steel. *Mater. Sci. Eng. A* **2009**, *509*, 31–40. [CrossRef]
9. Kreimeyer, M.; Wagner, F.; Vollertsen, F. Laser processing of aluminum–titanium-tailored blanks. *Opt. Laser Eng.* **2005**, *43*, 1021–1035. [CrossRef]
10. Shah, L.H.; Ishak, M. Review of research progress on aluminum–steel dissimilar welding. *Mater. Manuf. Process.* **2014**, *29*, 928–933. [CrossRef]
11. Shao, L.; Shi, Y.; Huang, J.K.; Wu, S.J. Effect of joining parameters on microstructure of dissimilar metal joints between aluminum and galvanized steel. *Mater. Des.* **2015**, *66*, 453–458. [CrossRef]
12. Borrisutthekul, R.; Yachi, T.; Miyashita, Y.; Mutoh, Y. Suppression of intermetallic reaction layer formation by controlling heat flow in dissimilar joining of steel and aluminum alloy. *Mater. Sci. Eng. A* **2007**, *467*, 108–113. [CrossRef]
13. Chen, S.H.; Huang, J.H.; Ma, K.; Zhang, H.; Zhao, X. Influence of a Ni-foil interlayer on Fe/Al dissimilar joint by laser penetration welding. *Mater. Lett.* **2012**, *79*, 296–299. [CrossRef]
14. Huang, J.K.; He, J.; Yu, X.Q.; Li, C.L.; Fan, D. The study of mechanical strength for fusion-brazed butt joint betweenaluminum alloy and galvanized steel by arc-assisted laser welding. *J. Manuf. Process.* **2017**, *25*, 126–133. [CrossRef]
15. Shi, Y.; Zhang, H.; Takehiro, W.; Tang, J.G. CW/PW dual-beam YAG laser welding of steel/aluminum alloy sheets. *Chin. J. Lasers* **2010**, *48*, 732–736.
16. Mei, S.W.; Gao, M.; Yan, J.; Zhang, C.; Li, G.; Zeng, X.Y. Interface properties and thermodynamic analysis of laser–arc hybrid welded Al/steel joint. *Sci. Technol. Weld. Join.* **2013**, *18*, 293–300. [CrossRef]
17. Gao, M.; Chen, C.; Mei, S.; Wang, L.; Zeng, X. Parameter optimization and mechanism of laser–arc hybrid welding of dissimilar al alloy and stainless steel. *Int. J. Adv. Manuf. Technol.* **2014**, *74*, 199–208. [CrossRef]

18. Dharmendra, C.; Rao, K.P.; Wilden, J.; Reich, S. Study on laser welding–brazing of zinc coated steel to aluminum alloy with a zinc based filler. *Mater. Sci. Eng. A* **2011**, *528*, 1497–1503. [CrossRef]
19. Laukant, H.; Wallmann, C.; Korte, M.; Glatzel, U. Flux-less joining technique of aluminium with zinc-coated steel sheets by a dual-spot-laser beam. *Adv. Mater. Res.* **2005**, *6–8*, 163–170. [CrossRef]
20. Zhou, D.W.; Liu, J.S.; Lu, Y.Z.; Xu, S.H. Effect of adding powder on joint properties of laser penetration welding for dual phase steel and aluminum alloy. *Opt. Laser Technol.* **2017**, *94*, 171–179. [CrossRef]
21. Chen, R.; Wang, C.L.; Jiang, P.; Shao, X.; Zhao, Z.; Gao, Z.; Yue, C. Effect of axial magnetic field in the laser beam welding of stainless steel to aluminum alloy. *Mater. Des.* **2016**, *109*, 146–152. [CrossRef]
22. Seffer, O.; Springer, A.; Kaierle, S. Investigations on remote laser beam welding of dissimilar joints of aluminum alloys and steel with varying sheet thicknesses for car body construction. *J. Laser Appl.* **2017**, *29*, 022414. [CrossRef]
23. Kouadri-David, A. Study of metallurgic and mechanical properties of laser welded heterogeneous joints between dp600 galvanised steel and aluminium 6082. *Mater. Des.* **2014**, *54*, 184–195. [CrossRef]
24. Sun, J.H.; Qi, Y.; Gao, W.; Huang, J. Investigation of laser welding on butt joints of al/steel dissimilar materials. *Mater. Des.* **2015**, *83*, 120–128.
25. Zhang, M.J.; Chen, G.Y.; Zhang, Y.; Wu, K.R. Research on microstructure and mechanical properties of laser keyhole welding–brazing of automotive galvanized steel to aluminum alloy. *Mater. Des.* **2013**, *45*, 24–30. [CrossRef]
26. Sun, J.H.; Huang, J.; Yan, Q.; Li, Z.G. Fiber laser butt joining of aluminum to steel using welding-brazing method. *Int. J. Adv. Manuf. Technol.* **2016**, *85*, 2639–2650. [CrossRef]
27. Zhu, Z.T.; Wan, Z.D.; Li, Y.X.; Chen, H. Intermediate layer, microstructure and mechanical properties of aluminum alloy/stainless steel butt joint using laser-MIG hybrid welding-brazing method. *Int. J. Mod. Phys. B* **2017**, *31*, 1744035. [CrossRef]
28. Salminen, A. The filler wire—Laser beam interaction during laser welding with low alloyed steel filler wire. *Mechanika* **2010**, *37*, 67–74.
29. Tomashchuk, I.; Sallamand, P.; Cicala, E.; Peyre, P.; Grevey, D. Direct keyhole laser welding of aluminum alloy AA5754 to titanium alloy Ti6Al4V. *J. Mater. Process. Technol.* **2015**, *217*, 96–104. [CrossRef]
30. Casalino, G.; Mortello, M.; Peyre, P. Yb–yag laser offset welding of aa5754 and t40 butt joint. *J. Mater. Process. Technol.* **2015**, *223*, 139–149. [CrossRef]
31. Zhou, L.; Li, Z.Y.; Song, X.G.; Tan, C.W.; He, Z.Z.; Huang, Y.X.; Feng, J.C. Influence of laser offset on laser welding-brazing of al/brass dissimilar alloys. *J. Alloys Compd.* **2017**, *717*, 78–92. [CrossRef]
32. Majumdar, B.; Galun, R.; Weisheit, A.; Mordike, B.L. Formation of a crack-free joint between ti alloyand al alloy by using a high-power $CO_2$ laser. *J. Mater. Sci.* **1997**, *32*, 6191–6200. [CrossRef]
33. Cui, L.; He, D.Y.; Fu, G.; Li, X.Y.; Jiang, J.M. Effect of fiber laser–mig hybrid process parameters on weld bead shape and tensile properties of commercially pure titanium. *Mater. Manuf. Process.* **2010**, *25*, 1309–1316.
34. Sánchez-Amaya, J.M.; Delgado, T.; De Damborenea, J.J.; Lopez, V.; Botana, F.J. Laser welding of AA 5083 samples by high power diode laser. *Sci. Technol. Weld. Join.* **2013**, *14*, 78–86.
35. Bouche, K.; Barbier, F.; Coulet, A. Intermetallic compound layer growth between solid iron and molten aluminium. *Mater. Sci. Eng. A* **1998**, *249*, 167–175. [CrossRef]
36. Leonardo, A.; Dominique, E.; Christian, H.S.; Arenholz, E.; Jank, N.; Bruckner, J.; Pyzalla, A.R. Intermetallic FexAly-phases in a steel/Al-alloy fusion weld. *J. Mater. Sci.* **2007**, *42*, 4205–4214.
37. Shi, H.X.; Qiao, S.; Qiu, R.F.; Zhang, X.J.; Yu, H. Effect of welding time on the joining phenomena of diffusion welded joint between aluminum alloy and stainless steel. *Mater. Manuf. Process.* **2012**, *27*, 1366–1369. [CrossRef]
38. Dybkov, V.I. Interaction of 18Cr-10Ni stainless steel with liquid aluminium. *J. Mater. Sci.* **1990**, *25*, 3615–3633. [CrossRef]
39. Miao, Y.G.; Han, D.F.; Yao, J.Z.; Li, F. Microstructure and interface characteristics of laser penetration brazed magnesium alloy and steel. *Sci. Technol. Weld. Join.* **2013**, *15*, 97–103. [CrossRef]
40. Sierra, G.; Peyre, P.; Deschaux-Beaume, F.; Stuart, D.; Fras, G. Steel to aluminium key-hole laser welding. *Mater. Sci. Eng. A* **2007**, *447*, 197–208. [CrossRef]
41. Bouayad, A.; Gerometta, C.; Belkebir, A.; Ambari, A. Kinetic interactions between solid iron and molten aluminium. *Mater. Sci. Eng. A* **2003**, *363*, 53–61. [CrossRef]

42. Nascimento, R.M.D.; Martinelli, A.E.; Buschinelli, A.J.A. Review article: Recent advances in metal-ceramic brazing artigo revisão: Avanços recentes em brasagem metal-cerâmica. *Cerâmica* **2003**, *49*, 178–198. [CrossRef]
43. Chen, J.; Li, J.; Amirkhiz, B.S.; Liang, J.; Zhang, R. Formation of nanometer scale intermetallic phase at interface of aluminum-to-steel spot joint by welding–brazing process. *Mater. Lett.* **2014**, *137*, 120–123. [CrossRef]
44. Springer, H.; Kostka, A.; Santos, J.F.D.; Raabe, D. Influence of intermetallic phases and kirkendall-porosity on the mechanical properties of joints between steel and aluminium alloys. *Mater. Sci. Eng. A* **2011**, *528*, 4630–4642. [CrossRef]